Journal of Solid State Chemistry **145,** 668–677 (1999)
Article ID jssc.1998.8280, available online at http://www.idealibrary.com on IDEAL®

Structure and Properties of YbZnSn, YbAgSn, and Yb_2Pt_2Pb

Rainer Pöttgen,* Petra E. Arpe,* Claudia Felser,† Dirk Kußmann,* Ralf Müllmann,‡ Bernd D. Mosel,‡ Bernd Künnen,* and Gunter Kotzyba*

*Anorganisch-Chemisches Institut, Universität Münster, Wilhelm-Klemm-Straße 8, D-48149 Münster, Germany; †Institut für Anorganische Chemie, Johannes Gutenberg-Universität, BecherWeg 24, D-55099 Mainz, Germany; and ‡Institut für Physikalische Chemie, Universität Münster, Schloßplatz 4/7, D-48149 Münster, Germany

E-mail: pottgen@uni-muenster.de; felser@indigotrem1.chemie.uni-mainz.de; mosel@uni-muenster.de

Received January 12, 1999; in revised form March 9, 1999; accepted March 13, 1999

YbZnSn, YbAgSn, and Yb_2Pt_2Pb were synthesized by reacting the elements in sealed tantalum tubes in a high-frequency furnace. The structures of YbAgSn and Yb_2Pt_2Pb were refined from single crystal X-ray data: YbAgPb type, $P\bar{6}m2$, $a = 479.2(2)$ pm, $c = 1087.3(3)$ pm, w$R2 = 0.050$, BASF = 0.34(8), 509 F^2 values, 18 variables for YbAgSn and Er_2Au_2Sn type, $a = 776.0(1)$ pm, $c = 701.8(2)$ pm, w$R2 = 0.072$, 426 F^2 values, 18 variables for Yb_2Pt_2Pb. The lattice constants of YbZnSn are confirmed: NdPtSb type, $P6_3mc$, $a = 464.7(1)$ pm, $c = 747.7(2)$ pm. The stannides YbZnSn and YbAgSn crystallize with superstructures of the AlB_2 type. The zinc (silver) and tin atoms form ordered Zn_3Sn_3 and Ag_3Sn_3 hexagons, respectively. The stacking sequences for the differently oriented hexagons are AB, AB for YbZnSn and ABC, ABC for YbAgSn. While exclusively Zn–Sn intralayer interactions were observed in YbZnSn, intralayer Ag–Sn and significant Sn–Sn interlayer interactions at 318 pm occur in YbAgSn. The [ZnSn] and [AgSn] polyanions in YbZnSn and YbAgSn, respectively, have a pronounced two-dimensional character. This picture of chemical bonding in YbAgSn is confirmed by TB–LMTO–ASA band structure calculations. The partial densities-of-states and the valence charge densities are discussed. The magnetic (no long-range ordering, Yb^{2+}) and the resistivity measurements (metallic behavior) are in excellent agreement with the electronic structure calculations. Yb_2Pt_2Pb crystallizes with the Er_2Au_2Sn structure, a ternary derivative of the Zr_3Al_2 type. This structure is composed of distorted AlB_2 and CsCl related slabs of compositions $YbPt_2$ and $YbPb$. Yb_2Pt_2Pb shows paramagnetic behavior ($4.3 \pm 0.4\ \mu_B$/Yb) indicating trivalent ytterbium. Magnetic susceptibility measurements on YbZnSn and YbAgSn show Pauli paramagnetism with room temperature susceptibilities of $2.5(1) \times 10^{-9}$ and $4.6(1) \times 10^{-9}$ m^3/mol. Electrical resistivity measurements indicate metallic conductivity with specific resistivities of 440 ± 40 μΩcm (YbZnSn) and 490 ± 40 μΩcm (YbAgSn) at 300 K. ^{119}Sn Mössbauer spectra of YbZnSn show a single signal at room temperature with an isomer shift of $\delta = 1.85(1)$ mm/s. YbAgSn shows two superimposed signals at 78 K: a singlet at $\delta = 1.94(1)$ mm/s and a second signal at $\delta = 1.99(1)$ mm/s subjected to quadrupole splitting of $\Delta E_Q = 1.35(1)$ mm/s, in agreement with the two crystallographically different tin sites. © 1999 Acamedic Press

Key Words: **intermetallic compounds; crystal structure; chemical bonding; ytterbium; ^{119}Sn Mössbauer spectroscopy.**

INTRODUCTION

Intermediate valence phenomena of rare earth containing materials have most intensively been investigated for cerium and europium based compounds, whereas only a few ytterbium-based systems have been studied (1). In the case of ytterbium, the different valence states correspond to the configurations $[Xe]4f^{14}$ (Yb^{2+}) and $[Xe]4f^{13}$ (Yb^{3+}). Besides mixed valency this degeneracy can lead to phenomena such as Kondo lattices or heavy fermion behavior.

Structural phase transitions accompanied by a valence change (Yb^{3+} in the low temperature and Yb^{2+} in the high temperature modification) have recently been observed for α- and β-YbPdSn (2) and α- and β-$YbAgGa_2$ (3). Stable trivalent ytterbium occurs in the ZrNiAl-type compounds YbNiAl (4) and YbPtSn (5, 6) which order antiferromagnetically at $T_N = 2.9$ and 3.5 K, respectively. Mixed or intermediate valence phenomena were found in Yb_3Si_5 (7, 8), $YbPd_2Si_2$ (9), $Yb_2Pt_3Sn_5$ (6), and several equiatomic ytterbium transition metal aluminides (10, 11).

In the course of our studies on structure–property relationships of intermetallic europium and ytterbium compounds (3, 6, 8, and ref. therein), we have now investigated the physical properties of the stannides YbZnSn and YbAgSn. The structure of YbZnSn has recently been refined from single crystal X-ray data (12), while only X-ray powder data have been reported for YbAgSn (5, 13, 14). The structure refinements of the latter stannide and of the new plumbide Yb_2Pt_2Pb are reported in the present paper. A brief account of some of this work was given recently at a conference (15).

0022-4596/99 $30.00

EXPERIMENTAL

Starting materials for the preparation of YbZnSn, YbAgSn, and Yb_2Pt_2Pb were ingots of ytterbium (Kelpin), zinc granules (Merck), silver wire (Degussa, $\varnothing$ 2 mm), platinum powder (Degussa, 200 mesh), tin ingots (Heraeus), and lead rods (Johnson–Matthey), all with stated purities better than 99.9%. Pure samples of the respective compounds were prepared by high-frequency melting (Kontron Roto-Melt, 1.2 kW) of the elements in the ideal atomic ratios in sealed tantalum tubes under flowing argon in a water-cooled sample chamber. The argon was purified over silica gel, molecular sieves, and titanium sponge (900 K). The experimental setup is described in detail in Ref. (6). In a first step, the tubes were heated with the maximum power output of the high-frequency generator. The strongly exothermic reactions are easily visible by the occurrence of white heat for about 2 s. The annealing temperature was then lowered to $\sim$1100 K for about 1 min and then raised again to the maximum. Subsequently the tubes were annealed for 1 h at about 900 K. These reactions resulted in light gray polycrystalline samples of YbZnSn, YbAgSn, and Yb_2Pt_2Pb which could easily be separated from the tantalum tubes.

The samples were routinely analyzed by EDX measurements using a Leica 420 I scanning electron microscope with platinum, tin, silver, zinc, PbF_2, and YbF_3 as standards. No impurity elements heavier than sodium were detected and the analyses were in good agreement with the ideal compositions. Tantalum contaminations from the container materials could thus safely be ruled out.

While the samples of YbZnSn and YbAgSn were single phase materials, the samples of the initial compositions Yb : Pt : Pb = 2 : 2 : 1 contained only about 90% Yb_2Pt_2Pb besides small amounts of a second and third ternary phase with the approximate compositions $\sim$YbPtPb and $\sim YbPtPb_2$ (determined by EDX). These plumbides have not yet been obtained in the form of small single crystals suitable for a structure determination.

YbZnSn, YbAgSn, and Yb_2Pt_2Pb are quite sensitive against moisture. The samples were therefore kept in Schlenk tubes and all manipulations were carried out under dried argon. The compounds are dark gray as fine-grained powders. Single crystals have metallic luster.

Guinier powder patterns of the samples were recorded with Cu$K\alpha_1$ radiation using α-quartz ($a = 491.30$ pm, $c = 540.46$ pm) as an internal standard. Both YbAgSn and Yb_2Pt_2Pb crystallize with pronounced subcells: a small hexagonal AlB_2 type subcell for YbAgSn and a small tetragonal U_3Si_2 type subcell for Yb_2Pt_2Pb. Additional weak reflections required a tripling (YbAgSn) and doubling (Yb_2Pt_2Pb), respectively, of the unit cells. The lattice constants (see Table 1) were obtained from least-squares fits of the Guinier data. To assure correct indexing, the observed patterns were compared with calculated ones (16) taking the atomic positions from the structure refinements. The Guinier powder data of YbAgSn and Yb_2Pt_2Pb are listed in Table 2. The strongest superstructure reflections are clearly resolved on the powder patterns. The powder data of YbZnSn were in perfect agreement with the results from Ref. (12).

TABLE 1
Lattice Constants of YbZnSn, YbAgSn, and Yb_2Pt_2Pb

Compound	a (pm)	c (pm)	c/a	V (nm^3)	Reference
YbZnSn	464.9(1)	747.6(1)	1.608	0.1399	(12)
YbZnSn	464.7(1)	747.7(2)	1.609	0.1398	This work
YbAgSn	479.1	725.6	1.515	0.1442	(13)
YbAgSn	478.8(1)	1087.0(1)	2.270	0.2158	(14)
YbAgSn	479.0	1088.7	2.273	0.2163	(5)
YbAgSn	479.2(2)	1087.3(3)	2.269	0.2162(1)	This work
Yb_2Pt_2Pb	776.0(1)	701.8(2)	0.904	0.4226(1)	This work

Single crystal intensity data were collected at room temperature by use of a four-circle diffractometer (CAD4) with graphite monochromatized Mo$K\alpha$ (71.073 pm) radiation and a scintillation counter with pulse height discrimination. The scans were taken in the $\omega/2\theta$ mode and empirical absorption corrections were applied on the basis of psi-scan data.

The magnetic susceptibilities of polycrystalline pieces of YbZnSn, YbAgSn, and Yb_2Pt_2Pb were measured with a SQUID magnetometer (MPMS, Quantum Design, Inc.) between 2 and 300 K with magnetic flux densities up to 5 T. The specific resistivities of YbZnSn and YbAgSn were determined on small irregularly shaped blocks (typical dimensions $1 \times 1 \times 2$ mm^3) with a conventional four-probe technique. Cooling and heating curves measured between 4.2 and 300 K were identical within the error bars.

^{119}Sn Mössbauer spectroscopic experiments were performed at room temperature and at 78 K on the same polycrystalline samples as used for the susceptibility and resistivity measurements. $Ca^{119m}SnO_3$ was taken as source and a palladium foil of 0.05 mm thickness was used to reduce the tin K X-rays concurrently emitted by the source.

Charge density and density of states calculations for YbAgSn were performed with the TB–LMTO–ASA method (17–19), an ab initio program for solids. Within this scalar relativistic method all relativistic effects except spin orbit coupling were taken into account. The calculations were performed within the local density and the local spin density approximation with the exchange-correlation potential of Barth and Hedin (20) to investigate whether or not a magnetic ground state is the stable one. All k-space integrations for the 296 irreducible k-points within the Brillouin zone were performed with the tetrahedron method (21). The basis set consisted of s, p d, and f orbitals for Yb, Ag, and Sn.

TABLE 2
Guinier Powder Data (Cu$K\alpha_1$ Radiation) for YbAgSn and Yb_2Pt_2Pb

h	k	l	$2\theta_o$	d_c (Å)	d_o (Å)	I_c	I_o
				YbAgSn			
0	0	2*	16.26	5.4363	5.4466	< 1	vw
1	0	0	21.44	4.1496	4.1406	3	w
1	0	1*	22.99	3.8768	3.8658	1	vw
0	0	3	24.57	3.6242	3.6199	3	w
1	0	2*	27.03	3.2985	3.2957	2	w
1	0	3	32.78	2.7297	2.7296	100	vs
1	1	0	37.53	2.3958	2.3947	75	vs
1	0	4*	39.62	2.2738	2.2730	3	w
2	0	0	43.62	2.0748	2.0731	< 1	vw
1	1	3	45.32	1.9986	1.9994	3	w
1	0	5*	47.14	1.9261	1.9262	2	vw
0	0	6	50.34	1.8121	1.8110	9	m
2	0	3	50.65	1.8006	1.8008	32	s
1	0	6	55.29	1.6607	1.6600	1	vw
2	0	4*	55.68	1.6492	1.6494	1	vw
1	1	6	64.36	1.4453	1.4463	30	s
2	1	3	64.68	1.4394	1.4399	35	s
3	0	0	67.69	1.3832	1.3830	17	m
2	1	4*	69.09	1.3585	1.3583	1	vw
				Yb_2Pt_2Pb			
1	1	0	16.12	5.4870	5.4936	3	w
1	0	1*	16.98	5.2050	5.2184	1	vw
0	0	2	25.35	3.5090	3.5110	8	w
1	1	2	30.19	2.9562	2.9575	3	vw
2	2	0	32.58	2.7435	2.7459	12	m
2	0	2	34.44	2.6025	2.6016	30	s
2	2	1*	35.08	2.5552	2.5558	2	vw
2	1	2	36.37	2.4674	2.4678	100	vs
3	1	0	36.57	2.4539	2.4548	60	s
3	1	1*	38.82	2.3164	2.3176	2	vw
3	2	0	41.93	2.1522	2.1529	10	m
1	1	3		2.1519		1	
3	1	2	45.04	2.0109	2.0110	13	m
4	0	0	46.79	1.9400	1.9401	5	w
4	1	0	48.27	1.8820	1.8839	5	w
3	2	2	49.64	1.8346	1.8349	10	m
0	0	4	52.03	1.7545	1.7561	14	m
4	2	0	52.72	1.7351	1.7349	6	w
3	0	3		1.7350		1	
4	1	2	55.31	1.6585	1.6596	9	m
3	3	2	56.71	1.6219	1.6219	6	w
5	1	0	60.83	1.5218	1.5215	5	w
2	2	4	62.86	1.4781	1.4771	4	w
4	1	3*	63.39	1.4664	1.4661	2	vw
3	1	4	65.33	1.4272	1.4272	26	s
5	1	2	67.00	1.3962	1.3956	18	m

Note. Visual intensities are given in units of vs (very strong), s (strong), m (medium), w (weak), and vw (very weak). Calculated intensities were generated with Lazy-Pulverix (16) using the positional parameters of the refined structures. Unambiguous superstructure reflections are marked by asterisks.

The Yb p, the Ag f, and the Sn d and f orbitals were treated by a down-folding technique (22). No empty spheres were necessary to fill the Wigner–Seitz cell with an intersphere overlap of less than 17%. The resulting radii of the different spheres were found to be $s_{Yb} = 3.74$ and 3.96, $s_{Ag} = 2.86$ and 2.89, and $s_{Sn} = 3.18$ and 3.22. For more detailed information about the calculation procedure we refer to (17–19).

RESULTS AND DISCUSSION

Structure Refinements

Irregularly shaped single crystals of YbAgSn and Yb_2Pt_2Pb were isolated from the annealed samples and examined by use of a Buerger camera. The precession photographs of YbAgSn (reciprocal layers $h0l$ and $h1l$) showed a small AlB_2-type hexagonal subcell. Additional weak reflections required a tripling of the lattice parameter c. No systematic extinctions were observed. This led to the space groups $P6/mmm$, $P\bar{6}2m$, and $P\bar{6}m2$, of which the noncentrosymmetric group $P\bar{6}m2$ was found to be correct during the structure refinements. The Yb_2Pt_2Pb crystal was characterized through the reciprocal layers $hk0$ and hhl. The superstructure reflections which required the doubling of the lattice parameter c were weak but all clearly visible on the reciprocal layer hhl. The systematic extinctions were compatible with space group $P4_2/mnm$ in agreement with our previous results on Er_2Au_2Sn (23). All relevant crystallographic data and experimental details for the data collections are listed in Table 3.

The atomic parameters of YbAgPb (14) and Er_2Au_2Sn (23) were taken as starting values and both structures were refined using SHELXL-97 (24) (full-matrix least-squares on F^2) with anisotropic atomic displacement parameters for all atoms. The latter were well behaved for Yb_2Pt_2Pb and for the ytterbium atoms of YbAgSn. The silver and tin sites of YbAgSn showed displacement parameters U_{33} which were up to five times larger than $U_{11} = U_{22}$. These displacements were more pronounced for the silver than for the tin sites. Since these displacements might be indicative for a violation of the mirror planes at $z = 0$ and $z = 1/2$, we also refined the YbAgSn structure in space group $P3m1$, a *translationengleiche* subgroup of index 2 of $P\bar{6}m2$. Actually CaLiSn (26) and CaAgPb (14) crystallize with this space group. The symmetry reduction did not improve the displacement parameters and further resulted in higher residuals and large correlations. The z parameters of Ag2 and Sn2 did not deviate from the ideal values by more than one standard deviation. In view of this result we prefer to describe the structure of YbAgSn in the higher symmetry space group $P\bar{6}m2$, in agreement with the recent results for isotypic YbAgPb (14). The anisotropic displacements of the silver and tin atoms in the superstructure might also be a result of the still strongly dominating subcell reflections. As a check for the correct site assignment (silver and tin differ only by

TABLE 3
Crystal Data and Structure Refinement for YbAgSn and Yb_2Pt_2Pb

Empirical formula	YbAgSn	Yb_2Pt_2Pb
Formula weight	399.60 g/mol	943.45 g/mol
Crystal system	hexagonal	tetragonal
Space group	$P\bar{6}m2$ (No. 187)	$P4_2/mnm$ (No. 136)
Lattice constants	see Table 1	see Table 1
Formula units per cell	$Z = 3$	$Z = 4$
Calculated density	9.21 Mg/m^3	14.83 Mg/m^3
Crystal size	$12 \times 12 \times 60\ \mu m^3$	$30 \times 25 \times 15\ \mu m^3$
Transmission (max/min)	2.05	2.44
Absorption coefficient	47.1 mm^{-1}	149.3 mm^{-1}
F (000)	501	1512
θ range for data collection	2° to 38°	2° to 33°
Range in hkl	$\pm 8, \pm 8, \pm 18$	$-11 \le h \le -2$, $\pm 11, +10$
Total no. reflections	5009	1269
Independent reflections	509 ($R_{int} = 0.058$)	426 ($R_{int} = 0.103$)
Reflections with $I > 2\sigma(I)$	408 ($R_{sigma} = 0.022$)	290 ($R_{sigma} = 0.080$)
Data/restraints/parameters	509/0/18	426/0/18
Goodness-of-fit on F^2	1.192	1.030
Final R indices [$I > 2\sigma(I)$]	$R1 = 0.020$	$R1 = 0.036$
	$wR2 = 0.044$	$wR2 = 0.064$
R indices (all data)	$R1 = 0.033$	$R1 = 0.073$
	$wR2 = 0.050$	$wR2 = 0.072$
R (subcell reflections)[a]	$182 > 2\sigma(F)$, $R1 = 0.014$	$190 > 2\sigma(F)$, $R1 = 0.032$
R (supercell reflections)[a]	$260 > 2\sigma(F)$, $R1 = 0.050$	$131 > 2\sigma(F)$, $R1 = 0.069$
BASF	0.34(8)	—
Extinction coefficient	0.0065(3)	0.0015(2)
Largest diff. peak and hole	2.69 and -2.11 e/Å^3	4.58 and -4.86 e/Å^3

[a] These values were calculated with the program RWERT (25) using the formula $\sum|F_o - F_c|/\sum|F_o|$.

TABLE 4
Atomic Coordinates and Isotropic Displacement Parameters (pm^2) for YbAgSn and Yb_2Pt_2Pb

Atom	Wyckoff site	x	y	z	U_{eq}
		YbAgSn (space group $P\bar{6}m2$)			
Yb1	2g	0	0	0.3333(1)	127(2)
Yb2	1a	0	0	0	140(3)
Ag1	2h	1/3	2/3	0.1849(3)	213(4)
Ag2	1f	2/3	1/3	1/2	275(8)
Sn1	2i	2/3	1/3	0.1461(2)	105(3)
Sn2	1d	1/3	2/3	1/2	143(4)
		Yb_2Pt_2Pb (space group $P4_2/mnm$)			
Yb1	4f	0.1801(2)	x	0	62(4)
Yb2	4g	0.3414(2)	$-x$	0	65(4)
Pt	8j	0.37274(8)	x	0.2717(1)	64(3)
Pb	4d	0	1/2	1/4	77(3)

Note. U_{eq} is defined as one third of the trace of the orthogonalized U_{ij} tensor.

three electrons) the occupancy parameters of the silver and tin sites were refined in a separate series of least-squares cycles along with the displacement parameters. No substantial deviation from the ideal composition was observed (all sites were fully occupied within two standard deviations) and in the final cycles the ideal occupancy parameters were assumed. A refinement of the Flack parameter (27, 28) indicated twinning by inversion. Subsequently the inversion twin matrix was introduced and a batch scale factor was refined to BASF = 0.34(8).

The final difference Fourier syntheses of YbAgSn was flat (Table 3), while a residual peak of 4.58 e/Å^3 was observed for Yb_2Pt_2Pb. The latter, however, was too close to the lead position (156 pm) to be indicative of an additional atomic site. It most likely resulted from an incomplete absorption correction. The positional parameters and interatomic distances of the refinements are listed in Tables 4 and 5. Although the structure refinements converged to low residuals, we prefer to calculate separate R-values for the superstructure reflections (see Table 3). The low residuals of $R = 0.050$ (YbAgSn) and $R = 0.069$ (Yb_2Pt_2Pb) for the superstructure reflections, assuming a 2σ cutoff, reflect the high quality of the data sets. Listings of the observed and calculated structure factors are available.[1]

Magnetic and Electrical Properties

The temperature dependence of the magnetic susceptibility of YbZnSn and YbAgSn is shown in Fig. 1, To check for ferromagnetic impurities the field dependence of each sample was also determined. Only negligible amounts of such impurities were detected: in both cases the 3 and the 5 T data were practically identical and we have therefore plotted the 3 T data. YbZnSn and YbAgSn are Pauli paramagnetic with room temperature values of $2.5(1) \times 10^{-9}$ m^3/mol (YbZnSn) and $4.6(1) \times 10^{-9}$ m^3/mol (YbAgSn). The increases of the susceptibilities at low temperatures arise from paramagnetic contributions, most likely minor amounts of impurities. We have therefore evaluated the susceptibility data according to the Curie law $\chi = C/T$. Since the plots of the inverse susceptibilities (Fig. 1) crossed the origin, no paramagnetic Curie temperature (Θ) needs to be applied. A rough estimation of these data according to $\mu_{exp} = (8C)^{1/2}\ \mu_B$ resulted in experimental magnetic moments of 0.7 μ_B (YbZnSn) and 0.9 μ_B (YbAgSn). Since the type and the atomic percentage of the impurity phases in YbZnSn and YbAgSn are unknown, the calculated moments are only an approximation. In view of the theoretical magnetic moments of 0 μ_B/Yb (Yb^{2+}) and

[1] Details may be obtained from: Fachinformationszentrum Karlsruhe, D-76344 Eggenstein-Leopoldshafen (Germany), by quoting the Registry No's. CSD-410744 (YbAgSn) and CSD-410745 (Yb_2Pt_2Pb).

TABLE 5
Interatomic Distances (pm) Calculated with the Lattice Constants Taken from X-Ray Powder Data of YbAgSn and Yb_2Pt_2Pb

	YbAgSn			Yb_2Pt_2Pb			
Yb1:	3	Ag1	320.3	Yb1:	2	Pt	284.7
	3	Ag2	330.7		4	Pt	290.3
	3	Sn2	330.7		4	Pb	334.6
	3	Sn1	343.5		2	Yb2	351.7
	1	Yb2	362.4		2	Yb2	391.8
	1	Yb1	362.5		1	Yb1	395.3
	6	Yb1	479.2		2	Yb2	423.6
Yb2:	6	Sn1	319.0	Yb2:	2	Pt	284.4
	6	Ag1	342.0		4	Pt	293.5
	2	Yb1	362.4		4	Pb	340.8
	6	Yb2	479.2		1	Yb2	348.1
					2	Yb1	351.7
Ag1:	3	Sn1	279.9		2	Yb1	391.8
	3	Yb1	320.3		2	Yb1	423.6
	3	Yb2	342.0				
	1	Sn2	342.6	Pt:	1	Pt	279.3
					1	Yb2	284.4
Ag2:	3	Sn2	276.7		1	Yb1	284.7
	6	Yb1	330.7		2	Yb1	290.3
	2	Sn1	384.9		2	Yb2	293.5
					2	Pb	306.0
Sn1:	3	Ag1	279.9		1	Pt	320.5
	1	Sn1	317.6		1	Pt	381.4
	3	Yb2	319.0				
	3	Yb1	343.5	Pb:	4	Pt	306.0
	1	Ag2	384.9		4	Yb1	334.6
					4	Yb2	340.8
Sn2:	3	Ag2	276.7		2	Pb	350.9
	6	Yb1	330.7				
	2	Ag1	342.6				

Note. Standard deviations are all equal or less than 0.3 pm. All distances shorter than 575 pm (Yb–Yb, Yb–Ag, Yb–Sn), 470 pm (Sn–Sn), 450 pm (Ag–Sn), and 400 pm (Ag–Ag) for YbAgSn, and 540 pm (Yb–Pb, Pb–Pb), 510 pm (Yb–Yb, Yb–Pt), 450 pm (Pt–Pb), and 425 pm (Pt–Pt) for Yb_2Pt_2Pb are listed.

4.54 μ_B/Yb (Yb^{3+}), according to $\mu_{eff} = g[J(J+1)]^{1/2}$, the ytterbium atoms in these stannides are essentially divalent.

Although our best samples of Yb_2Pt_2Pb contained only about 90% of the desired phase, we nevertheless investigated the magnetic behavior in order to know whether the ytterbium atoms are divalent or trivalent. An evaluation of the straight line of the plot of the inverse susceptibility (measured at 3 *T* from 100 to 300 K) resulted in a paramagnetic Curie temperature $\Theta = -21 \pm 4$ K and an experimental moment of $\mu_{eff} = 4.3 \pm 0.4\ \mu_B$/Yb. The large standard deviations of μ_{exp} and Θ account for the inaccuracy of the data evaluation. Nevertheless, the results of the magnetic measurement indicate essentially trivalent ytterbium in Yb_2Pt_2Pb.

The temperature dependence of the specific resistivity of YbZnSn and YbAgSn is shown in Fig. 2. Due to the irregular surface of the samples, the absolute values of the specific resistivities varied slightly from sample to sample. We have therefore plotted the normalized specific resistivities $\rho(T)/\rho(300\ \text{K})$. This also allows a better comparison of the two compounds. For both stannides the specific resistivity decreases with decreasing temperature as is usual for metallic conductors. The room temperature values are $\rho = 440 \pm 40\ \mu\Omega$cm (YbZnSn) and $\rho = 490 \pm 40\ \mu\Omega$cm (YbAgSn). The error limits account for the values obtained for different samples. The resistivity ratios $\rho(4.2\ \text{K})/\rho(300\ \text{K})$ are 0.30 for YbZnSn and 0.54 for YbAgSn. A similar temperature dependence of the resistivity was recently also observed for the two modifications of YbPdSn (2) and for $Yb_2Pt_3Sn_5$ (6). The resistivity and susceptibility data for YbAgSn are in agreement with those reported recently in Ref. (5).

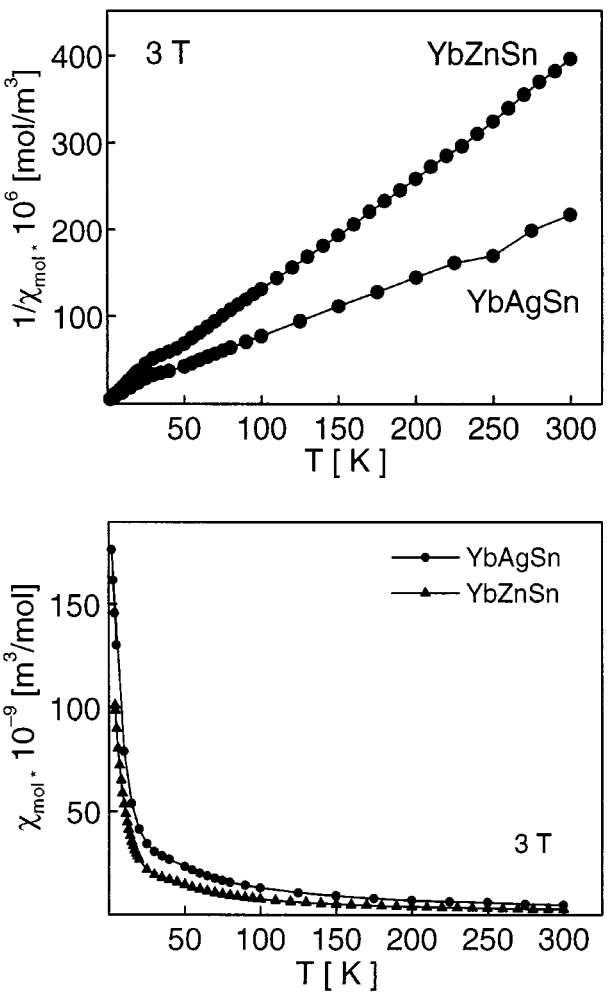

FIG. 1. Temperature dependence of the inverse magnetic susceptibility (top) and the magnetic susceptibility (bottom) of YbZnSn and YbAgSn determined at an external field of B = 3T.

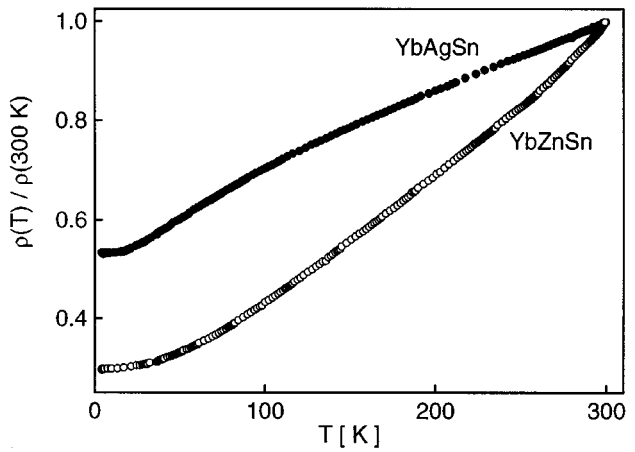

FIG. 2. Temperature dependence of the resistivity ratio $\rho(T)/\rho$ (300 K) of YbZnSn and YbAgSn.

^{119}*Sn Mössbauer Spectroscopy*

The room temperature ^{119}Sn Mössbauer spectrum of YbZnSn is presented in Fig. 3. We observe one singlet (without quadrupole splitting) at an isomer shift of $\delta = 1.85(1)$ mm/s and an experimental line width of $\Gamma = 0.91(2)$ mm/s. This is in agreement with the single tin site determined from the single crystal X-ray experiment (12).

The 78 K spectrum of YbAgSn is more complex. Here we observe a superposition of two signals: a singlet at $\delta = 1.94(1)$ mm/s with a line width of $\Gamma = 0.77(2)$ mm/s and an electrical field gradient of $-0.43(1)$ mm/s and a second signal at $\delta = 1.99(1)$ mm/s with a line width of $\Gamma = 0.84(3)$ mm/s subjected to quadrupole splitting of $\Delta E_Q = 1.35(1)$ mm/s. The integrated peak areas (singlet : doublet) are about 1 : 2.2, in agreement with the multiplicities of the tin sites (1*d* for Sn2 and 2*i* for Sn1). The occurrence of quadrupole splitting for the 2*i* site of the tin atoms of the Sn1 dumbbell is in agreement with the lower site symmetry (3*m*.) when compared with the higher site symmetry ($\bar{6}m2$) for the *isolated* tin atom.

The isomer shifts of YbZnSn and YbAgSn are in the typical range for such intermetallic compounds: 1.84(2) mm/s for α-YbPdSn (2), 1.96(4) mm/s for β-YbPdSn (2), 1.75(1) mm/s for YbPtSn (6), and 2.02(1) mm/s for $Yb_2Pt_3Sn_5$ (6).

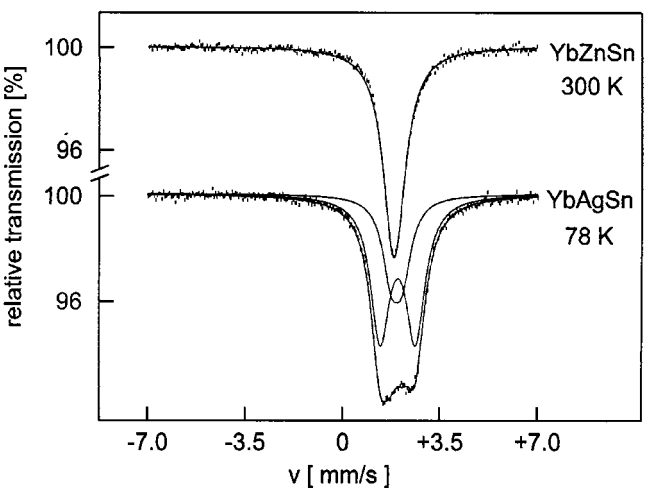

FIG. 3. Experimental and simulated ^{119}Sn Mössbauer spectra of YbZnSn (300 K) and YbAgSn (78 K).

Crystal Chemistry and Chemical Bonding

The structures of YbZnSn (12) and YbAgSn (Fig. 4) are derived from the well-known AlB_2 type. The zinc (silver) and tin atoms form ordered $[Zn_3Sn_3]$ and $[Ag_3Sn_3]$ hexagons, respectively, which show different stacking sequences. Although the structure of YbZnSn has been refined recently (12), chemical bonding in this stannide was not discussed. The fully ordered $[Zn_3Sn_3]$ hexagons are slightly puckered and every other hexagon is rotated by 60° with respect to each other, resulting in a stacking sequence AB, AB. Within the networks the Zn–Sn distances are 276 pm, only slightly larger than the sum of the Pauling single bond radii (29) of 265 for zinc and tin. The interlayer Zn–Sn distances of 311 pm are even much longer than the sum of the metallic radii for coordination number (CN) 12 (30) of 302 pm. Similar Zn–Sn distances have recently been determined for EuZnSn (31, 32) with orthorhombic TiNiSi type structure: 278 pm intralayer and 305 pm interlayer Zn–Sn distances. According to the course of the interatomic distances we observe strong intralayer and much weaker interlayer Zn–Sn bonding in YbZnSn. Considering the magnetic data (essentially divalent ytterbium), the formula of this stannide may to a first approximation be written as $Yb^{2+}Zn^{2+}Sn^{4-}$. In emphasizing the predominantly covalent bonding in the

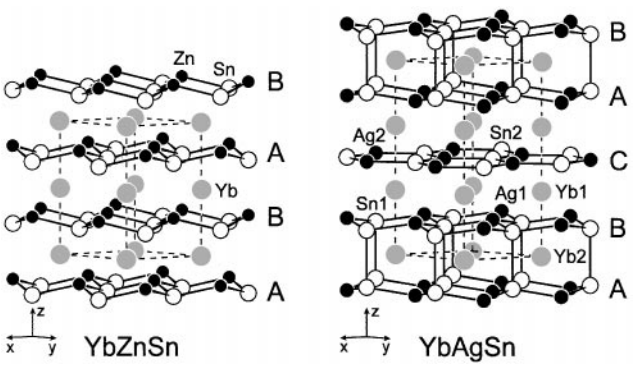

FIG. 4. The crystal structures of YbZnSn (drawn with the parameters of Ref. (12)) the YbAgSn. The two-dimensional [ZnSn] and the two different two-dimensional [AgSn] networks are emphasized.

pronounced two-dimensional polyanion we can also write $Yb^{2+}[ZnSn]^{2-}$. Chemical bonding in such NdPtSb and LiGaGe compounds was recently investigated by LMTO electronic structure calculations for the series of LnAuGe germanides (33).

YbAgSn is isotypic with YbAgPb (14). This peculiar structure (Fig. 4) shows a different stacking sequence for the ordered $[Ag_3Sn_3]$ hexagons. There occur two puckered and one planar $[Ag_3Sn_3]$ layer, resulting in the stacking sequence ABC, ABC. The Ag–Sn distances within these layers range from 277 (planar layer) to 280 pm (puckered layers), only slightly larger than the sum of Paulings single bond radii (29) of 274 pm for silver and tin indicating strong covalent Ag–Sn bonding within these layers. Chemical bonding between these layers is quite different. The superimposed layers A and B are puckered such a way that the tin atom can form Sn–Sn bonds between the layers with Sn–Sn distances of 318 pm. This distance is comparable to the Sn–Sn distances in β-tin, where each tin atom has four neighbors at 302 pm and two further neighbors at 318 pm (34). Also the structure of CaLiSn (26) has Sn_2 pairs with a Sn–Sn distance of 319 pm, while the interlayer Sn–Sn distances of 297 and 300 pm in the orthorhombic structures of CaAuSn (35) and EuAuSn (36) are smaller. The planar $[Ag_3Sn_3]$ layer is rotated by 60° with respect to the double layers. The resulting interlayer Ag–Sn distances of 343 and 385 pm are significantly longer than the respective intralayer distances. This clearly indicates that there are only minor Ag–Sn interactions between the layers C and B, and A, respectively. The structure of YbAgSn thus consists of two different two-dimensonally infinite $[Ag_6Sn_6]$ and $[Ag_3Sn_3]$ polyanions.

The Sn–Sn single bond distance of 281 pm is observed in the diamond modification of α-Sn (34). In organometallic compounds like distannanes the Sn–Sn distances vary from 276 to about 303 pm, depending on the steric effect of the substituents (37, 38). A much longer Sn–Sn distance of 363 pm is observed in $(2,4,6\text{-}(CF_3)_3C_6H_2)_2Sn\text{–}Sn(2,4,6\text{-}(CF_3)_3C_6H_2)_2$. This Sn–Sn interaction is certainly very weak, but it is responsible for dimerization of the molecule and furthermore, this interaction clearly appears in optical measurements (38). In view of these Sn–Sn, distances the Sn–Sn bond of 318 pm in YbAgSn may only be considered as a weak interaction. Assuming essentially divalent ytterbium (see magnetic data) and monovalent silver, the formula of YbAgSn may to a first approximation be described by $[3Yb^{2+}]^{6+}[3Ag^{+}]^{3+}[Sn]^{4-}[Sn_2]^{5-}$. This way the *isolated* tin atoms obtain the close [Xe] shell and the dimer has a charge of -5. Considering the slightly enhanced magnetic moment of 0.93 μ_B/Yb and the relatively long Sn–Sn distance, a formulation $[Yb^{2+}Yb^{2+}Yb^{3+}]^{7+}[3Ag^{+}]^{3+}[Sn]^{4-}[Sn_2]^{6-}$ would also be possible.

Chemical bonding in YbAgSn was investigated in more detail by TB–LMTO–ASA electronic structure calculations. As an overview we present the total density of states (DOS) of YbAgSn and some important partial DOS in Fig. 5. Due to the relative low density of states at the Fermi energy E_F (3.8 states per eV and unit cell) we expect neither a magnetic ground state nor mixed valent behavior (39). Also the spin polarized calculation leads to a nonmagnetic ground state, in excellent agreement with the experimental Pauli paramagnetic ground state. Both crystallographically different ytterbium sites are divalent with a f^{14} configuration. Although the *f* states are found only 0.3 eV below E_F (the small spike shown in the upper part of Fig. 5), they are separated from the other states and the states at E_F are dominated by the conduction electrons of this metallic compound. The *f* states are directly localized at the ytterbium atoms with an extremely small bandwidth as expected from the physical properties.

The states around -8 eV below E_F belong to the two crystallographically different tin sites. The *s* and *p* partial DOS of Sn1 and Sn2 are shown in the middle part of Fig. 5. The *s* states of Sn1 are split in two peaks separated by around 1 eV. From this splitting we can conclude that there seems to be a bonding interaction between adjacent Sn1

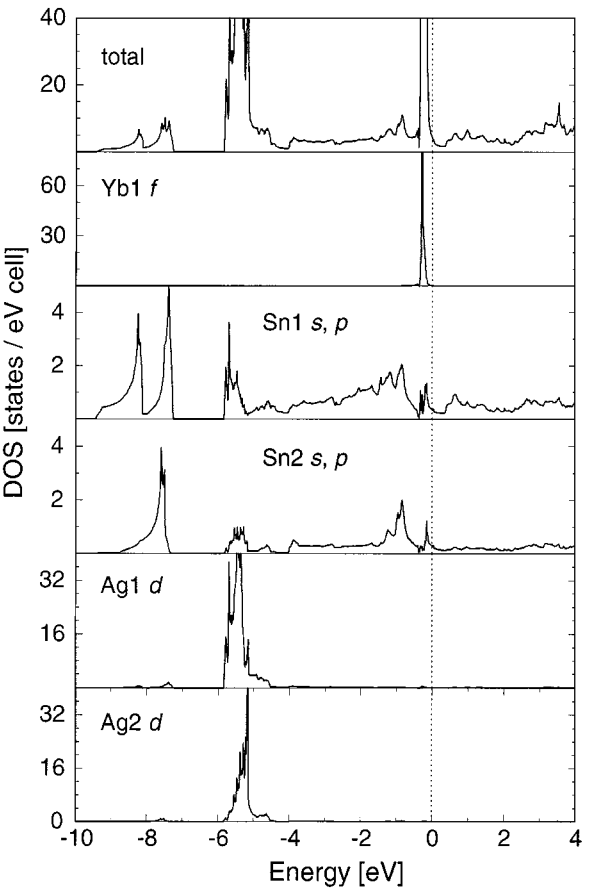

FIG. 5. Total and partial density-of-states (DOS) of YbAgSn.

atoms, leading to two nondegenerated bands, one with bonding and the other with antibonding character. This is in agreement with the crystal structure which shows $Sn1_2$ dumbbells and *isolated* Sn2 atoms. Therefore we observe only one *s* peak around −8 eV below E_F (which corresponds to one band) in the partial DOS of Sn2 (Fig. 5). The Sn1 and Sn2 *p* states are located between −6 eV and the Fermi energy. They have also some contributions above E_F. The states between −6 and −5 eV (in the range of the Ag *d* states shown below) result from bonding interactions with the silver atoms. The main contributions of the Sn *p* states are between −4 eV and E_F. These states dominate together with Yb *d* the states at E_F. The silver *d* states are located at the bottom of the valence band (Fig. 5). They are far away from E_F and well localized with a small band dispersion of only 1.5 eV.

Figure 6 presents a contour plot of the total valence charge distribution of YbAgSn. These plots show the varying intralayer and interlayer bonding. The electronic charge density enables us to verify our assumptions on bonding in this peculiar compound. The main features of the contour plot are strong Ag1–Sn1 and Ag2–Sn2 interactions in the puckered and in the planar AgSn nets with very similar charge densities. Perpendicular to these nets the situation is different. We observe only a large increase of the electronic charge between the Sn1 atoms (Fig. 6), indicating the presence of covalent Sn1–Sn1 bonding. The two crystallographically different ytterbium atoms seen at the edge and in the middle of the contour plot do not significantly interact with any other atom.

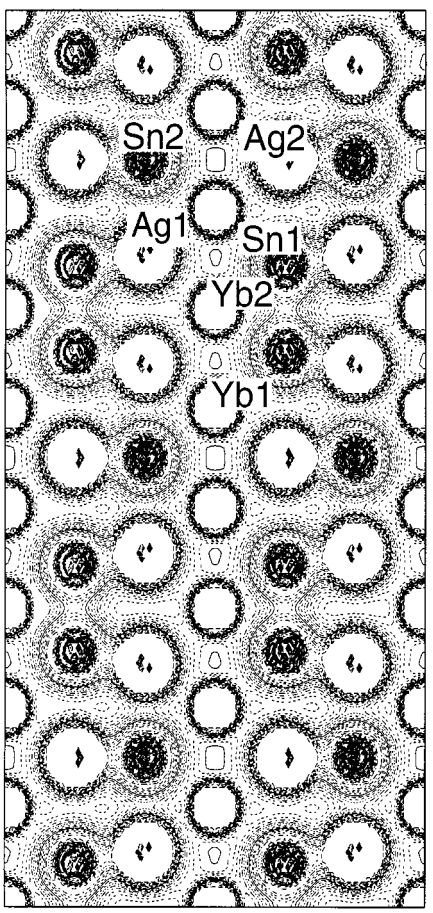

FIG. 6. Total valence charge distribution of YbAgSn in the [110] direction ($0.5 \le x, y \le 1.5$): 21 contours are drawn between 0 and 0.04 e/a_0^3 (a_0^3 is the Bohr radius).

As already mentioned above, the structure of YbAgSn (YbAgPb type) is derived from the aristotype AlB_2. The corresponding group–subgroup scheme is presented in Fig. 7 in the compact and concise Bärnighausen formalism (40, 41). Starting from the aristotype AlB_2 a *translationengleiche* symmetry reduction of index 2 (*t*2) leads to the SrPtSb type structure (42) of space group $P\bar{6}m2$. This represents a completely ordered derivative of AlB_2 with planar Pt_3Sb_3 hexagons. The ordering of platinum and antimony expresses itself only in a change of the intensities of the subcell reflections (43). The second step leads to the YbAgPb structure by an *isomorphic* reduction of index 3 (*i*3) which results in the occurrence of superstructure reflections. This symmetry reduction further uncouples the silver and lead positions and allows a puckering of the hexagons. In the YbAgPb-type structure the Ag_3Pb_3 C layer is planar (Fig. 4). A further symmetry reduction, realized for CaLiSn (26) and CaAgPb (13), then allows also a puckering of this layer. CaLiSn crystallizes with space group *P*3*m*1, a *translationengleiche* subgroup of index 2 (*t*2) of $P\bar{6}m2$.

The new plumbide Yb_2Pt_2Pb crystallizes with the Er_2Au_2Sn type structure (23), a ternary ordered version of the Zr_3Al_2 type. The series of R_2T_2X (R = rare earth or actinoid metal, T = transition metal, X = element of the *p* block) compounds has intensively been investigated in the last five years since they exhibit a variety of interesting magnetic and electrical properties. An overview on the corresponding literature is given in Ref. (44).

As emphasized in Fig. 8, the Yb_2Pt_2Pb structure is composed of CsCl and AlB_2 related slabs of compositions *YbPb* and $YbPt_2$. Compounds with these compositions, however, crystallize with different structures: YbPb (45) adopts the CuAu type and $YbPt_2$ (46) crystallizes with the structure of the cubic Laves phase $MgCu_2$. Within the AlB_2-like slab the Pt–Pt distance is 279 pm, only slightly larger than the Pt–Pt distance of 277 pm in *fcc* platinum (34). The CsCl-like slab is strongly distorted. The average edge length for the cube ground plane is about 408 pm and the respective *c* parameter is 352 pm (half the lattice constant *c*), leading to a significantly compressed cube. This way each lead atom has four Yb1 neighbors at 335 pm and four Yb2 neighbors at 341 pm. In YbPb with CuAu-type structure the near neighbor environment of the lead atom is also tetragonally distorted, but now the *c* parameter of 444 pm is significantly

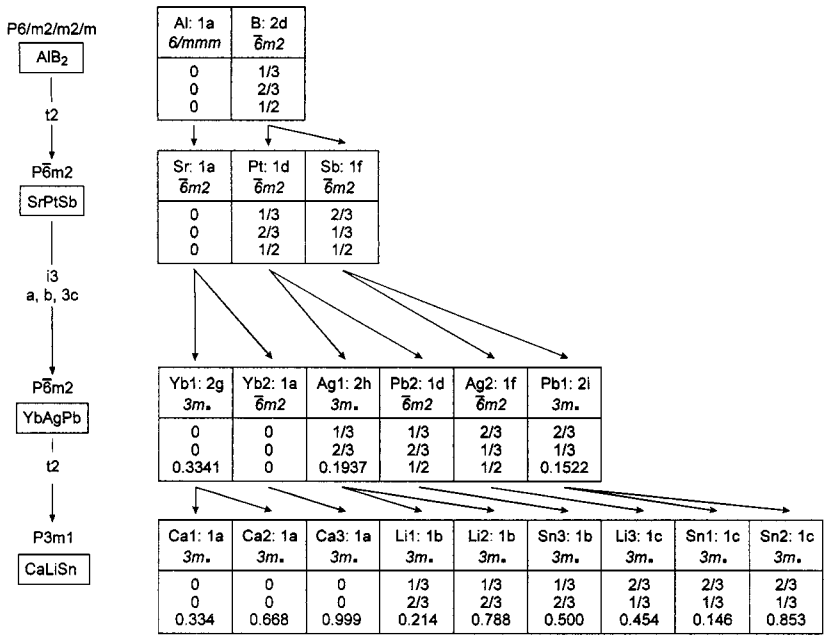

FIG. 7. Group-subgroup relationship (40, 41) for the structures of YbAgPb and CaLiSn starting from the aristotype AlB_2. The indices of the *translationengleiche* (*t*) and isomorphic (*i*) transitions, as well as the unit cell tranformations are given.

larger than the *a* parameter of 360 pm. This results in eight equal Yb–Pb distances of 338 pm.

The Yb–Pt distances range from 284 to 294 pm, significantly smaller than in the Laves phase $YbPt_2$ (46) where each ytterbium atom has twelve platinum neighbors at 306 pm. Also the Yb–Yb distances of 348 and 351 pm in Yb_2Pt_2Pb are shortened when compared with *fcc* ytterbium (388 pm) (34). In addition to the eight ytterbium neighbors each lead atom has four platinum neighbors at 306 pm capping the rectangular sites of the distorted cubes. In view of the sum of the single bond radii (29) of 283 pm for lead and platinum, the Pt–Pb interactions in Yb_2Pt_2Pb are only weakly bonding. Also in the binary phases PtPb (47) with NiAs structure and Pt_3Pb (48) with Cu_3Au structure the Pt–Pb distances of 281 and 287 pm, respectively, are smaller. The Pb–Pb contacts between adjacent CsCl slabs (351 pm) have also some bonding character. These Pb–Pb distances are comparable to *fcc* lead (350 pm) (34). This picture of chemical bonding is in agreement with a recent extended Hückel calculation for Sc_2Ni_2In (44). Here the strongest bonding interactions were found for the Sc–Ni contacts followed by Sc–In and Ni–In. This model may also be valid for Yb_2Pt_2Pb.

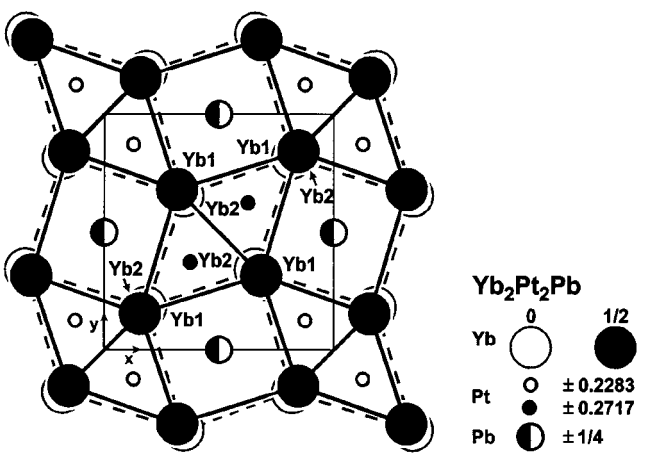

FIG. 8. Projection of the crystal structure of Yb_2Pt_2Pb along the *c* axis. The CsCl- and AlB_2-like slabs are emphasized.

The ytterbium atoms are by far the less electronegative component of Yb_2Pt_2Pb. Unfortunately, no value for the absolute electronegativity is given in Pearson's list (49). Since the chemical behavior of ytterbium is similar to that of calcium (2.2 eV) and strontium (2.0 eV), a similar value can safely be assumed also for ytterbium. The absolute electronegativities of 5.6 eV for platinum and 3.9 eV for lead are larger. In view of the trivalent character of the ytterbium atoms (see magnetic data above), a formulation of Yb_2Pt_2Pb according to $[2Yb^{3+}]^{6+}[2Pt^{-}]^{2-}[Pb]^{4-}$ is a first approximation.

ACKNOWLEDGMENTS

We are grateful to Prof. W. Jeitschko and Prof. H. Eckert for their interest and steady support. We are also indebted to Dipl.-Ing. U. Ch.

Rodewald for the data collections on the four circle diffractometer, to K. Wagner for the EDX measurements, and to Dr. W. Gerhartz (Degussa AG) for a generous gift of noble metals. This work was financially supported by the Fonds der Chemischen Industrie and Deutsche Forschungsgemeinschaft (Po-573/1-2).

REFERENCES

1. A. Szytuła and J. Leciejewicz, "Handbook of Crystal Structures and Magnetic Properties of Rare Earth Intermetallics," CRC Press, Boca Raton, FL, 1994.
2. D. Kußmann, R. Pöttgen, B. Künnen, G. Kotzyba, R. Müllmann, and B. D. Mosel, *Z. Kristallogr.* **213,** 356 (1998).
3. Yu. Grin, M. Ellner, K. Hiebl, B. Baumgartner, and P. Rogl, *J. Alloys Compd.* **221,** 125 (1995).
4. C. Schank, G. Olesch, J. Köhler, U. Tegel, U. Klinger, J. Diehl, S. Klimm, G. Sparn, S. Horn, C. Geibel, and F. Steglich, *J. Magn. Magn. Mater.* **140–144,** 1237 (1995).
5. K. Katoh, T. Takabatake, A. Minami, I. Oguro, and H. Sawa, *J. Alloys Compd.* **261,** 32 (1997).
6. R. Pöttgen, A. Lang, R.-D. Hoffmann, B. Künnen, G. Kotzyba, R. Müllmann, B. D. Mosel, and C. Rosenhahn, *Z. Kristallogr.* **214,** 143 (1999).
7. A. Iandelli, A. Palenzona, and G. Olcese, *J. Less-Common Met.* **64,** 213 (1979).
8. R. Pöttgen, R.-D. Hoffmann, and D. Kußmann, *Z. Anorg. Allg. Chem.* **624,** 945 (1998).
9. E. V. Sampathkumaran, K. H. Frank, G. Kalkowski, G. Kaindl, M. Domke, and G. Wortmann, *Phys. Rev. B* **29,** 5702 (1984).
10. G. Cordier, T. Friedrich, R. Henseleit, A. Grauel, U. Tegel, C. Schank, and C. Geibel, *J. Alloys Compd.* **201,** 197 (1993).
11. C. Schank, U. Tegel, R. Henseleit, A. Grauel, G. Olesch, C. Geibel, G. Cordier, R. Kniep, and F. Steglich, *J. Alloys Compd.* **207/208,** 333 (1994).
12. F. Merlo, M. Pani, and M. L. Fornasini, *J. Alloys Compd.* **171,** 329 (1991).
13. D. Mazzone, D. Rossi, R. Marazza, and R. Ferro, *J. Less-Common Met.* **80,** P47 (1981).
14. F. Merlo, M. Pani, and M. L. Fornasini, *J. Alloys Compd.* **232,** 289 (1996).
15. R. Pöttgen, R.-D. Hoffmann, D. Kußmann, and P. E. Arpe, "First International Conference on Inorganic Materials, Versailles, 16–19 September 1998," Abstract G10.
16. K. Yvon, W. Jeitschko, and E. Parthé, *J. Appl. Crystallogr.* **10,** 73 (1977).
17. O. K. Andersen, *Phys. Rev. B.* **12,** 3060 (1975).
18. O. K. Andersen and O. Jepsen, *Phys. Rev. Lett.* **53,** 2571 (1984).
19. O. K. Andersen, O. Jepsen, and D. Götzel, *in* "Highlights of Condensed-Matter Theory" (F. Bassani, F. Furi, and M. P. Tosi, Eds.). North-Holland, New York, 1985.
20. U. von Barth and L. Hedin, *J. Phys. C* **5,** 1629 (1972).
21. O. Jepsen and O. K. Andersen, *Solid State Commun.* **9,** 1763 (1971).
22. G. Krier, O. K. Andersen, and O. Jepsen, unpublished results.
23. R. Pöttgen, *Z. Naturforsch.* **49b,** 1309 (1994).
24. G. M. Sheldrick, "SHELXL-97, Program for Crystal Structure Refinement." University of Göttingen, Germany, 1997.
25. R.-D. Hoffmann, "RWERT, Program for the Calculation of Residuals for Different Classes of Reflections." University of Münster, Germany, 1996.
26. W. Müller and R. Voltz, *Z. Naturforsch.* **29b,** 163 (1974).
27. H. D. Flack, *Acta Crystallogr., Sect. A* **39,** 876 (1983).
28. G. Bernadinelli and H. D. Flack, *Acta Crystallogr., Sect. A* **41,** 500 (1985).
29. L. Pauling, "The Nature of the Chemical Bond and The Structures of Molecules and Crystals," Cornell University Press, Ithaca, 1960.
30. E. Teatum, K. Gschneidner Jr., and J. Waber, Rep. LA - 2345, 1960 (US Department of Commerce, Washington, DC).
31. R. Pöttgen, *Z. Kristallogr.* **211,** 884 (1996).
32. U. Ernet, R. Müllmann, B. D. Mosel, H. Eckert, R. Pöttgen, and G. Kotzyba, *J. Mater. Chem.* **7,** 255 (1997).
33. R. Pöttgen, H. Borrmann, C. Felser, O. Jepsen, R. Henn, R. K. Kremer, and A. Simon *J. Alloys Compd.* **235,** 170 (1996).
34. J. Donohue, "The Structures of the Elements." Wiley, New York, 1974.
35. D. Kußmann, R.-D. Hoffmann, and R. Pöttgen, *Z. Anorg. Allg. Chem.* **624,** 1727 (1998).
36. R. Pöttgen, R.-D. Hoffmann, R. Müllmann, B. D. Mosel, and G. Kotzyba, *Chem. Eur. J.* **3,** 1852 (1997).
37. K. M. Mackay, *in* "The Chemistry of Organic Germanium, Tin and Lead Compounds" (S. Patai, Ed.), Chap. 2, Wiley, Chichester, 1995.
38. M. Driess and H. Grüzmacher, *Angew. Chem.* **108,** 900 (1996).
39. C. Felser, *J. Alloys Compd.* **262–263,** 87 (1997).
40. H. Bärnighausen, *Commun. Math. Chem.* **9,** 139 (1980).
41. H. Bärnighausen and U. Müller, "Symmetriebeziehungen zwischen den Raumgruppen als Hilfsmittel zur straffen Darstellung von Strukturzusammenhängen in der Kristallchemie." University of Karlsruhe and University Gh Kassel, Germany, 1996.
42. G. Wenski and A. Mewis, *Z. Anorg. Allg. Chem.* **535,** 110 (1986).
43. J. H. Albering, R. Pöttgen, W. Jeitschko, R.-D. Hoffmann, B. Chevalier, and J. Etourneau, *J. Alloys Compd.* **206,** 133 (1999).
44. R. Pöttgen and R. Dronskowski, *Z. Anorg. Allg. Chem.* **622,** 355 (1996).
45. G. Bruzzone and F. Merlo, *J. Less-Common Met.* **48,** 103 (1976).
46. A. Iandelli and A. Palenzona, *J. Less-Common Met.* **43,** 205 (1975).
47. N. N. Zhuravlev, G. S. Zhdanov, and Ye. M. Smirnova, *Phys. Metals Metallogr.* **13,** 55 (1962).
48. M. Ellner, *J. Less-Common Met.* **78,** P21 (1981).
49. R. G. Pearson, *Inorg. Chem.* **27,** 734 (1988).